This is a repository copy of *Predicting subsurface inclusion initiated butterfly-wing cracking under rolling contact fatigue*.

White Rose Research Online URL for this paper:
https://eprints.whiterose.ac.uk/id/eprint/231233/

Version: Published Version

Predicting subsurface inclusion initiated butterfly-wing cracking under rolling contact fatigue

R. Dai, H. Long *

Department of Mechanical Engineering, the University of Sheffield, Sheffield, UK

ABSTRACT

Wind turbine (WT) gearbox bearings experience premature failures. Damage characterisation of failed bearings has shown that subsurface micro cracks and butterfly-wing cracks are associated with non-metallic inclusions in the bearing raceways. The existing studies are unable to predict crack propagation under rolling contact fatigue considering shakedown and ratchetting when the material around an inclusion experiences sufficiently high levels of stresses. In this study, a finite element (FE) damage model based on the Continuum Damage Mechanics (CDM) is developed, integrated with the modelling of plastic deformation and kinematic hardening when the material around inclusion is subjected to alternating tension and compression. Two damage types of manganese-sulphide inclusions are investigated, showing significant effects of inclusion boundary separation and internal cracking on the subsurface RCF crack evolution. The modelling results also show that higher surface traction, overloads and varied loading sequences, commonly experienced by WTs in operation, have significant effects on the increase of the subsurface butterfly-wing crack lengths, because of early crack initiation and accelerated crack propagation. The developed CDM FE model has shown its effectiveness in predicting the damage evolution to gain new insights of complex interactions of a number of critical factors that can lead to the premature failure of bearings.

1. Introduction

Wind turbines (WTs) operate under varied wind speeds, sometimes under harsh weather and complex operating conditions. Reducing failures and downtimes of WTs will greatly reduce costs associated with operation and maintenance to achieve low-cost wind energy production. According to a study by the US Department of Energy, bearing problems were the most frequently observed issues, causing about 76 % of all the gearbox failures [1]. Damage related to bearings, such as the cracking [2], surface denting and pitting, were frequently observed on both the bearing raceways and rolling elements, and all of them had a negative impact on the bearing life [3]. It was reported that at least one-third of the WT gearboxes had experienced bearing failures within the operating period of 7 years, although these bearings were designed for 20 years' service life [4].

Rolling contact fatigue (RCF) is one of the most commonly observed failure modes in bearings due to the repeated stresses developed in contact surfaces between the rolling elements and the raceways [5]. RCF can be initiated either from the contact surface or subsurface. The damage initiation from the contact surface can be caused by plastic deformation of the surface asperities and/or the inadequate lubrication condition, resulting in surface micro pitting and spalling [6]. Different from the surface initiated RCF damage, the subsurface RCF damage is initiated at a depth below the contact surface, causing the material microstructural changes and micro cracks, often initiated by the non-metallic inclusions in the bearing steel [5]. Due to the stress concentration, micro cracks can initiate from these defects then propagate from the subsurface to reach the contact surface under the cyclic RCF loading to cause surface flaking, eventually resulting in the bearing failure.

The failure modes of the WT gearbox bearings have been intensively investigated in the past decade [4]. Considerable effort was devoted to investigate and understand the formation of White Etching Areas (WEAs) and White Etching Cracks (WECs) observed in the failed bearings [7,8]. The root causes and formation mechanisms of the WEAs and WECs which led to the premature failures of these bearings were highly debated [9,10]. Multiple drivers were identified [11,12] and the unique loading conditions of the WT operation and the contact stress history were considered to be a determining factor [13,14]. With the occurrence

of unavoidable complex loading conditions of WTs, due to wind speed variation, wind gust, turbine starting and braking, and electrical network grid faults, these caused slips of contact surfaces when underloaded as well as overloaded and at extremely loaded conditions [15]. Combined with the stress concentration around the inclusions located at the critical subsurface depths, small micro cracks were initiated from these defects and propagated to form butterfly-wing cracks at the inclusions and large crack networks in the subsurface areas [8,16,17]. Under the unique loading conditions of the WT operation, these cracks were propagated significantly faster to reach the surface of the bearing raceways causing the surface flaking, resulting in the premature bearing failure. A study by Richardson et al. [18] presented the clear evidence of the early stages of the WEC formation at the non-metallic inclusions in the subsurface; with increasing test duration the propagation of these cracks from the subsurface region to the contact surface was observed, eventually causing the surface flaking.

While a considerable progress has been made in identifying the non-metallic inclusions in the subsurface as one of the critical root causes of the formation of the WEAs and WECs under RCF, the findings from the current studies are unable to answer the question of why the non-metallic inclusions and the associated WEA and WEC damage have caused the significantly shorter RCF life of the WT gearbox bearings than any other applications. To answer this, the following critical factors have to be investigated:

(1) Why WEAs and WECs significantly reduce the fatigue life of the bearing steel. WEAs are microstructural damage caused by a phase transformation of the bearing steel from martensite to ferrite which reduces the toughness of the bearing steel because it becomes hardened due to the formation of the WEAs. Micro cracks, butterfly-wing cracks at the inclusions may be initiated due to alternating shear stresses in the localised subsurface area under repeated rolling contact. These cracks can form into large WEC networks and lead to White Structure Flaking (WSF) of the bearing raceway surface, as reported in [7–9]. Therefore it is important to investigate the effect of realistic loading conditions of the complex WT operation on the crack initiation and propagation at the inclusions and how it significantly shortens the bearing service life.

(2) It has been reported that the subsurface non-metallic inclusions had reduced both the fatigue endurance limit and the fracture toughness of the bearing steel [19,20]. These non-metallic inclusions are usually created from the non-metallic materials added during the steel manufacturing processes to aid the machining processes of the bearing. Due to the subsequent heat treatment and the unique WT operation, the non-metallic materials themselves may be damaged or voids may be created between the inclusions and the steel matrix. Thus it is critical to identify the inclusion damage types and investigate how the damaged inclusions can shorten the bearing life.

(3) WT gearbox bearings experience extremely high numbers of fatigue cycles due to the variable loads and variable speeds, and frequent dynamic loading conditions. Under the extreme loading, due to the stress concentration caused by the subsurface inclusions, the adjoining steel matrix may be subjected to plastic deformation during the rolling contact process. The steel material may be strain hardened which prevents the occurrence of further plastic deformation of the material, however this plastic deformation is not entirely beneficial. The steel matrix around the inclusion may experience the shakedown and ratcheting processes under RCF loading. It can reduce the fatigue endurance limit and the fracture toughness of the material and makes the steel matrix more brittle, contributing to the accelerated crack propagation.

To investigate these critical factors on the significantly shortened

RCF life of the WT gearbox bearings, the initiation and propagation of the cracks caused by damaged inclusions under realistic WT cyclic loads considering shakedown and ratchetting processes should be studied. The application of the Finite Element (FE) method provides a suitable solution for investigating the inclusion induced stress concentration, plastic deformation, and material kinematic hardening. However, the large volume of current publications are based on damage characterisation and experimental investigations, there are limited studies in modelling inclusion induced RCF damage development. Vincent et al. [19] suggested that the grain boundary dislocations at the inclusion-matrix interface caused by the plastic deformation could affect the formation of cracks. The FE model developed in this work estimated the movement and accumulation of dislocations around the high modulus inclusions after a certain number of rolling contact loading cycles. Alley and Neu [20] applied the FE modelling to determine the accumulation of the plastic strain in the steel matrix around the inclusion for predicting the butterfly-wing crack formation. It proposed a two-phase hybrid model which helped to determine the volumetric strain during the austenite-to-martensite phase transformation and the plastic strain accumulation during the rolling contact process. In another study by Ravi et al. [21], both Dang Van and Fatemi–Socie fatigue criteria were applied to model the RCF crack initiation at the MnS and Al_2O_3 inclusions. It concluded that the butterfly damage initiation was also governed by the traditional fatigue criteria. In recent studies by Mahdavi et al. [22,23] it was demonstrated numerically how micro plasticity, i.e. the yielding behaviour below the conventional 0.2 % plastic strain threshold, could lead to the initiation of cracks at the subsurface defects, in rolling contact applications operated under realistic loads. These numerical modelling methods have accurately predicted the locations of butterfly damage at the inclusions, however they are unable to determine the propagation directions of the subsurface cracks. Moghaddam et al. [24] proposed a damage model using Continuum Damage Mechanics (CDM) to simulate both the initiation and propagation of the subsurface butterfly-wing formations. By assuming the damage initiation process as the reduction of the material stiffness, their investigation successfully predicted the initiation positions and the propagation directions of the subsurface butterfly-wing damage. The findings obtained in [24] provided sufficient confidence that the CDM was a suitable and accurate method to simulate the subsurface RCF damage evolution. However, there are a number of challenges to overcome: to identify and model the damaged inclusions, to determine the plastic deformation in the adjoining steel matrix at the inclusions, and to model the RCF shakedown and ratcheting processes, when the bearings are subjected to the realistic WT loading conditions.

In this study, a FE damage model based on the Continuum Damage Mechanics (CDM) is developed. The aim is to develop an effective modelling method to predict the initiation and propagation of the fatigue cracks caused by subsurface inclusions under cyclic RCF loading. The developed damage model can consider the accumulation of plastic deformation and kinematic hardening of the bearing steel, capable of simulating the possible shakedown and ratchetting processes when the material at the inclusion is subjected to alternating tension and compression loading conditions in RCF. The typical operating conditions of WTs are modelled to investigate the effect of varied loading levels and loading sequences on the damage evolution. The effective and accurate damage modelling developed in this study supports the prediction of the accelerated RCF damage propagation by investigating specific inclusion damage types and complex loading conditions. New insights gained from the modelling and prediction can potentially improve strategies of bearing steel manufacturing and WT operation to reduce the bearing premature failure and the cost of wind energy.

2. Identification of inclusion damage types in the bearing steel

In the damage characterisation of the butterfly-wing cracks of the WT gearbox bearings in [8,16], it was observed that the inclusions were

not always perfectly bonded with the surrounding steel matrix. Due to the heat treatment of the steel and overloading or extreme loading conditions of the WT operation, the boundary separated inclusions and internally cracked inclusions were found in large numbers in the subsurface areas of the raceways of the failed bearings [16]. It was reported that both types of the inclusion damage were harmful to the crack propagation in the steel matrix and could easily cause the formation of the butterfly-wing cracks in the raceway subsurface [25].

To identify typical damaged inclusions in the subsurface, two failed planetary bearings of a 2 MW WT are investigated, shown in Fig. 1a. Samples cut from the raceways of the failed bearings are observed and analysed by optical microscopy and Scanning Electron Microscopy. Energy Dispersive X-ray spectroscopy analysis shows that 90 % of the inclusions found within the butterfly wing cracks is manganese-sulphide (MnS) inclusions. Microstructural observation has shown that the surface flaking of the raceways is often initiated from the subsurface RCF crack networks associated with damaged MnS inclusions. WEAs have been found to be decorated along the subsurface RCF cracks. Different forms of the damaged inclusions are identified, including (1) boundary separations between the inclusion and the steel matrix, (2) internal cracking of the inclusion, and (3) crack propagation from the inclusion into the steel matrix with or without WEAs.

Fig.1b, c and d show some examples of different forms of the damaged inclusions found in the samples cut from the two failed bearing raceways. It is observed when a subsurface inclusion is perfectly bonded with the steel matrix (Fig. 1b), it is less likely to cause significant damage to the bearing. The boundary separations of an inclusion (Fig. 1c) may be caused by the differences of the thermal expansion and contraction coefficients between the inclusion and the steel matrix during the steel heat treatment processes. The contact pressure acting on the raceway surface may also lead to the boundary separation because the inclusion-matrix ionic bonds may be broken due to the differences in deformation of the inclusion and the steel matrix. The internal cracking of the inclusion (Fig. 1d) is often caused by more complex mechanisms, including inclusion types and their chemical compositions, and energy released from thermal expansion and contraction because of the steel heat treatment. The internal cracks of an inclusion can also be propagated into the steel matrix (Fig. 1d) because of highly localised stresses at the crack tips and gaps at inclusion tips, especially if the geometry of an inclusion has an excessive length-to-width ratio. The damaged inclusions can result in the stress concentration, combined with the subsurface alternating shear stresses under RCF, it leads to the formation of cracks decorated with WEAs. They often have cracking damage shapes similar to butterfly wings, with single or double sets of wings, as shown in Fig. 1d.

3. Development of the CDM based FE damage model

This study focuses on investigating the effect of the subsurface stresses caused by different types of damaged inclusions on accelerating the RCF crack initiation and propagation under varying loading levels and load sequences in the typical WT operation. The following sections outline the key steps in the development of the CDM based FE damage model to investigate the three critical factors outlined in Section 1.

3.1. Damage evolution model under rolling contact fatigue

The deterioration or failure of a material can be considered as a
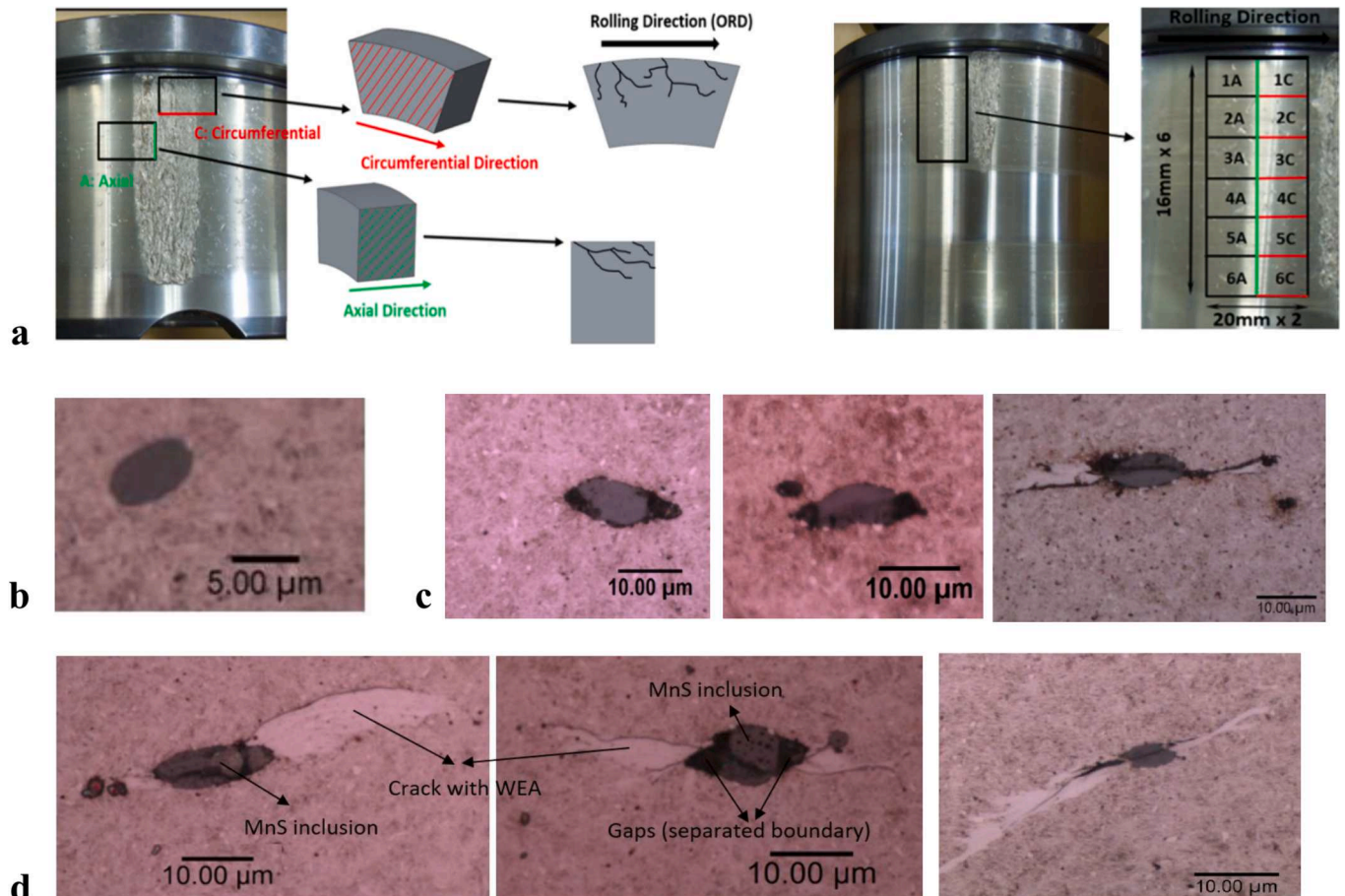
Fig. 1. Inclusion initiated damage of bearing raceways: (a) failed raceways and illustration of subsurface cracking networks; (b) a perfectly bounded inclusion; (c) inclusions with boundary separations; (d) inclusions with internal cracks and boundary separations, and butterfly-wing cracks propagated into steel matrix.

progressive loss of the material cross-sectional area under loading when the effective area able to carry the load is gradually reduced. Based on the isotropic damage theory, Kachanov [26] introduced the damage variable D thus the expression of a three-dimensional stress–strain field can be shown as:

$$\sigma_{ij} = C_{ijkl}(1 - D)\varepsilon_{kl} \tag{1}$$

where C_{ijkl} is the stiffness matrix of the elastic modulus of the material. A modified damage evolution model was proposed by Xiao et al. [27], expressed as:

$$\frac{dD}{dN} = \frac{\overline{B}}{q(1-D)^{2q}}\left(\sigma_{eqM}{}^{2q} - \sigma_{eqm}{}^{2q}\right) \tag{2}$$

This nonlinear equation solves the damage variable by an incremental method, where dD is the unit damage increment, dN is the unit increment of the number of loading cycles. σ_{eqM} is the maximum equivalent stress, and σ_{eqm} is the minimum equivalent stress. $\overline{B}$ and q are the material constants. To reduce the material parameters required, Wang et al. [28] proposed a simplified damage evolution model based on Xiao's model [27], expressed as:

$$\frac{dD}{dN} = \left[\frac{\sigma_{eqM}}{\sigma_r(1 - D)}\right]^m \tag{3}$$

The damage evolution rate is expressed by dD/dN; σ_r and m are the material constants; σ_r is known as the resistance stress representing the ability of the material to resist fatigue damage [28].

Considering the subsurface RCF damage due to inclusions is usually caused by the variation of the orthogonal shear stress, Raje et al. [29] and Li et al. [30] suggested to define the alternating orthogonal shear stress during the rolling contact process as the maximum equivalent stress σ_{eqM} in Eq.(3). Considering Goodman's relationship of the fatigue damage, both the stress amplitude and the stress mean of the alternating orthogonal shear stress were shown to make dominant contributions to the fatigue damage initiation [31]. For modelling the damage increment, Moghaddam et al. [24] proposed a new dominating stress considering both alternating and mean values of the orthogonal shear stress:

$$\frac{dD}{dN} = \left[\frac{\tau_{alternating} + |\tau_{mean}|}{\sigma_r(1 - D)}\right]^m \tag{4}$$

where τ_{mean} is the mean value of the orthogonal shear stress in the current loading cycle; $\tau_{alternating}$ is the half range of the alternating orthogonal shear stress which can be determined by the maximum and minimum orthogonal shear stresses during each loading cycle:

$$\tau_{alternating} = \frac{\tau_{maximum} - \tau_{minimum}}{2} \tag{5}$$

In addition to the study by Moghaddam et al. [24], the findings from other studies, such as [29,30,31,32], also concluded that the alternating orthogonal shear stress in the subsurface area was the dominating stress affecting the initiation of RCF cracking of the bearing raceway. Therefore, in this study, the orthogonal shear stress, under the effect of the surface traction due to RCF and the stress concentration at the damaged inclusions is determined to evaluate the RCF damage evolution.

3.2. Consideration of plastic deformation and kinematic hardening

As reviewed in Section 1, the plastic deformation of the steel matrix affects the fatigue damage accumulation. In this study, the incremental theory with the Levy-Mises flow rule is applied to calculate the stress and strain after the occurrence of material yielding. According to the flow rule, the material incremental strain can be described as [32]:

$$d\varepsilon_{ij} = d\varepsilon_{ij}^e + d\varepsilon_{ij}^p \tag{6}$$

where $d\varepsilon_{ij}$ is the total strain increment, $d\varepsilon_{ij}^e$ and $d\varepsilon_{ij}^p$ are the elastic and plastic strain increments, respectively. For the elastic stress increment, it can be expressed as:

$$d\sigma_{ij}^e = C_{ijkl}\left(d\varepsilon_{ij} - d\varepsilon_{ij}^p\right) \tag{7}$$

For the plastic strain increment $d\varepsilon_{ij}^p$, it can be expressed as:

$$d\varepsilon_{ij}^p = \frac{3}{2}\overline{d\varepsilon^p} \bullet \eta_{ij} = \frac{3}{2}\overline{d\varepsilon^p} \bullet \frac{\left(\sigma_{ij} - \sigma_{hydro}\delta_{ij}\right)}{\sigma_{eqv}} \tag{8}$$

where $\overline{d\varepsilon^p}$ is the equivalent plastic strain increment, η_{ij} is the flow stress tensor, σ_{ij} is the stress component tensor, σ_{hydro} is the hydrostatic stress, and σ_{eqv} is the von-Mises equivalent stress. δ_{ij} is the Kronecker delta: when $i = j$, $\delta_{ij} = 1$; when $i \neq j$, $\delta_{ij} = 0$.

It was well established that the Hertz contact pressure on the bearing raceway surface under rolling contact condition introduced the alternating tensile and compressive principal stresses to the areas affected by the stress concentration due to an inclusion [33]. When the WT gearbox bearings operate under the overloading conditions, the severe stress concentration of the steel matrix may cause the alternating shear stress exceeding the shear yielding stress of the material. Therefore, this may require the consideration of the Bauschinger effect of the material. The asymmetry of the yielding stress locus due to the Bauschinger effect can be modelled by the kinematic hardening of the material. The initial yielding surface of the material does not expand during the kinematic hardening process. Instead, it directly shifts with the direction of a vector α_{ij}, which is also known as the back stress. In the kinematic hardening, the yielding function takes the general form as:

$$f\left(\sigma_{ij} - \alpha_{ij}\right) = 0 \tag{9}$$

According to the results obtained by Chaboche [34], the expression of the increment of the back stress, $d\alpha_{ij}$, can be written as:

$$d\alpha_{ij} = E_t \bullet \overline{d\varepsilon^p} \bullet \frac{\sigma_{ij} - \alpha_{ij} - \sigma_{hydro}\delta_{ij}}{\sigma_{eqv}} \tag{10}$$

where E_t is the tangent modulus of the material after yielding.

In this study, the implementation of the developed damage evolution model into the FE simulation based on the CDM utilises the commercial FE software ABAQUS/CAE 2017 Standard. To define the cyclic load movement during rolling contact, the DLOAD and UTRACLOAD user subroutines are developed. The former defines the movement of the distributed Hertz contact pressure, and the latter defines the possible surface traction pressure caused by the friction between the contact surfaces. The stress updating and damage accumulation processes are completed by the user subroutine UMAT. Fig. 2 shows the relationship between each user subroutine and the computation sequence between them in the developed CDM based FE model for the RCF damage modelling.

4. FE damage modelling of bearing raceway

The bearing investigated in this study is the planetary bearing from the gearbox of a 2 MW wind turbine. According to the design parameters of the wind turbine and the gearbox design of three gear stages, the maximum contact pressure and half contact length of the inner raceway of the upwind planetary bearing under the rated condition is calculated as 2.069 GPa and 0.531 mm respectively by using the Hertz contact theory. The details of the design parameters and the calculation of the maximum Hertz contact pressure are provided in the Appendix.

4.1. FE model of bearing raceway and subsurface inclusion

Fig. 3(a) illustrates the contact between the raceway and rollers. Since the loading on the inner raceway is unevenly distributed, only the
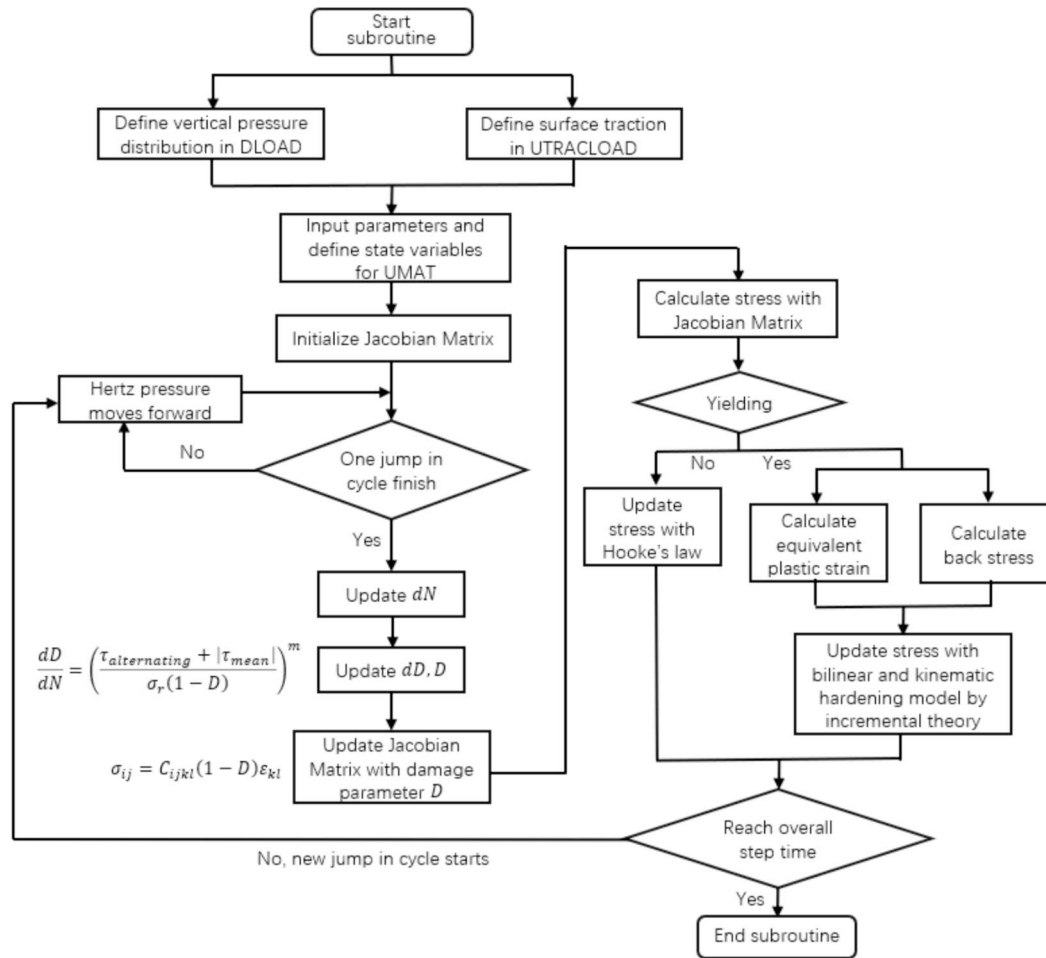
Fig. 2. Flowchart of the RCF damage modelling by ABAQUS user subroutines DLOAD, UTRACLOAD, and UMAT.

contact between the roller in the middle and the raceway, which induces the maximum loading, will be analysed in this study. As illustrated in Fig. 3(b), to create the FE model of a bearing raceway, the maximum contact pressure of 2.069 GPa and the half contact length of $b = 0.531$ mm are used (the calculation details are provided in the Appendix). The bearing raceway surface is simplified into a 2D rectangle plane in the FE model with the width of $4b$ and the length of $8b$, suggested in the study by Raje et al. [29]. Increasing the model size increases the computational time significantly due to the microscopic size of the inclusion and a number of non-linearity involved in the simulation. Using the selected dimensions of the 2D rectangle FE model, the curvature of the raceway surface can be ignored but it still provides a sufficient geometrical domain to prevent the effect of the boundary conditions of the model on the stresses around the inclusion. The elliptical distributed Hertz contact pressure is applied to the contact surface of the bearing raceway. When the distributed Hertz contact pressure moves from the left to the right over the inclusion, the 2D FE model can simulate the variation of the subsurface stresses near the inclusion changing from the minimum to the maximum. During one rolling contact cycle, the distributed Hertz contact pressure moves from the left to the right of the rectangle plane with a constant speed of $6b$ per second. As the rectangle plane representing the raceway surface length is $8b$, the overall modelling time is 1 s for each rolling contact cycle.

A MnS inclusion of an elliptical shape with an aspect ratio of two is placed in the subsurface of the raceway in the 2D FE model. The length of the inclusion along the major axis is 10 μm and along the minor axis is 5 μm. The inclusion is located in the middle of the rectangle plane of the raceway at a subsurface depth of 0.398 mm. This is the location of the

maximum shear stress of the raceway subsurface under the Hertz contact pressure applied. Using the material properties of the MnS inclusion provided in [35], the Young's Modulus of 120 GPa and the Poisson's ratio of 0.24 are defined in the 2D FE model. The yielding stress and maximum strength of the MnS inclusion are 325 MPa and 600 MPa respectively based on the nano-indentation results obtained in [36]. Considering the microscopic sizes of the inclusion, a fine mesh around the inclusion is required to obtain detailed and accurate FE modelling results of the stress distribution. A global FE model with relatively coarse meshes is established first to obtain the stress and strain results of the modelled raceway geometry. The local area around the inclusion is then created as a separated FE sub-model by using fine meshes. During the modelling process, the boundary conditions of the FE sub-model are interpolated by using the results from the global FE model. For both FE models, the elements are created by using the "free type" method with the medial axis algorithm for the 2D plane strain condition. As shown in Fig. 3(c) and Fig. 3(d), the size of the elements varies from 0.05 to 0.001 mm in the partition areas of the global model. However, the mesh sizes of the sub-model of the fine meshes have a maximum value of 1×10^{-4} mm and a minimum value of 3×10^{-5} mm.

To investigate the effect of the inclusion damage on RCF crack initiation and propagation, Fig. 4 defines three different types of boundary conditions of the inclusion to the steel matrix by considering both damaged and undamaged inclusions. In Fig. 4(a), the inclusion is perfectly bonded with the steel matrix, and it will not be separated from the matrix during the loading process. Fig. 4(b) shows the separated inclusion with two artificially created gaps at the inclusion tips. In this case, only part of the inclusion boundary is perfectly bonded with the
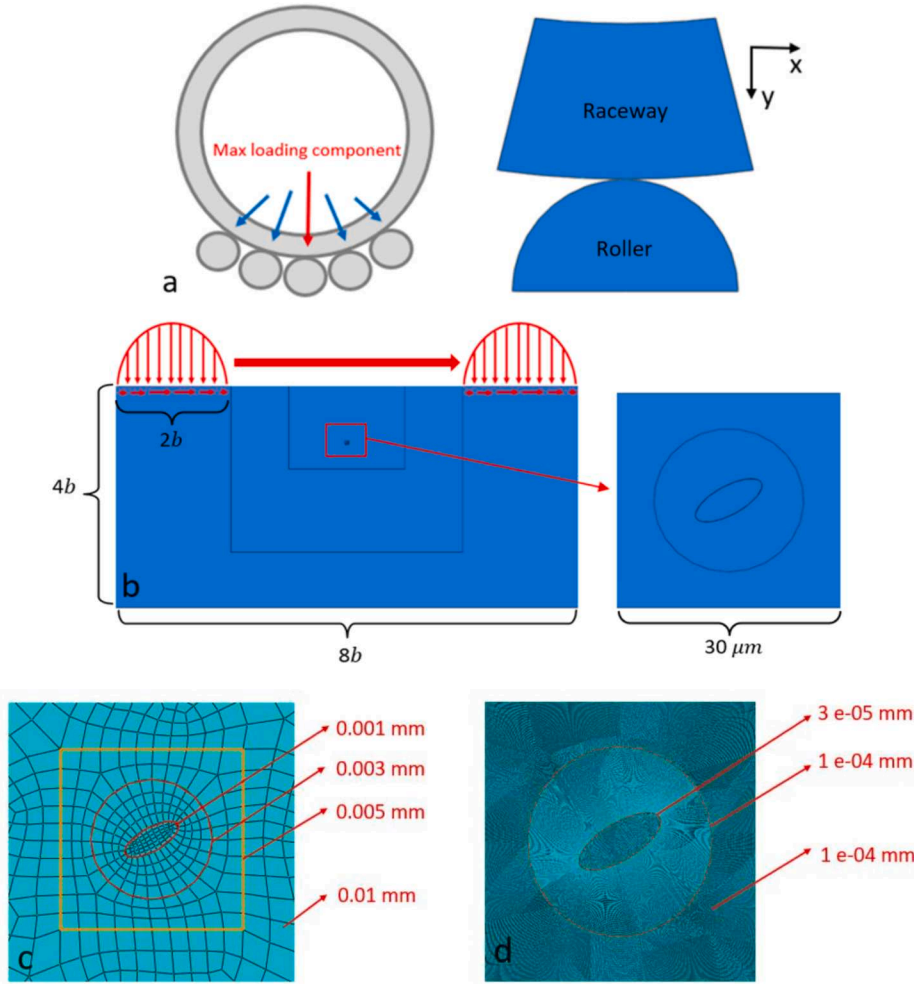
Fig. 3. Contact between the raceway and roller: (a) Contact forces between rollers and inner raceway. (b) Distributed Hertz contact pressure on raceway model with an MnS inclusion. (c) FE mesh of the global model. (d) FE mesh of the sub-model.
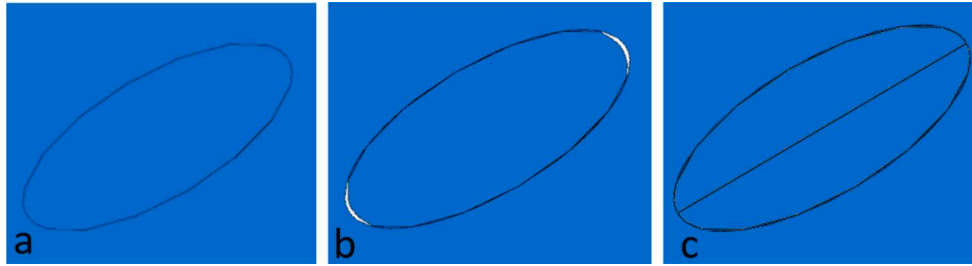
Fig. 4. Definition of the inclusion-steel matrix boundary conditions: (a) Perfectly bonded. (b) Boundary separation. (c) Internal cracked inclusion at 30°.

steel matrix. Fig. 4(c) defines an internal crack of the inclusion at 30° to the horizontal contact surface. Apart from the existence of the internal crack, the inclusion is perfectly bonded with the steel matrix, similar to the boundary condition defined in Fig. 4(a). Because the friction of the MnS is typically small, the contact between two broken parts of the inclusion is defined as a "hard" contact surface and frictionless in the FE model [37].

4.2. Material parameters for the damage modelling

To calibrate the material parameters of the damage model, Raje et al. [29] determined the material constant, m and σ_r by using the material SN-curve obtained from the torsional fatigue tests. The following

expressions are proposed in [29]:

$$m = B_1 \; and \; \sigma_r = 2\tau_{f1}(B_1 + 1)^{1/B_1} \tag{11}$$

where B_1 and τ_{f1} are the Basquin slope and the stress-axis intercept of the SN curve respectively. The bearing material investigated in this study is DIN 100Cr6, its torsional SN-curve is shown in Fig. 5 [29]. To calculate the Basquin slope B_1, the following equation can be used:

$$m = B_1 = \frac{\log(N_1) - \log(N_2)}{\log(S_2) - \log(S_1)} \tag{12}$$

where (N_1, S_1) and (N_2, S_2) are two points on the SN-curve, and both N_1 and N_2 should be larger than 10^4 cycles. Two points of loading cycles
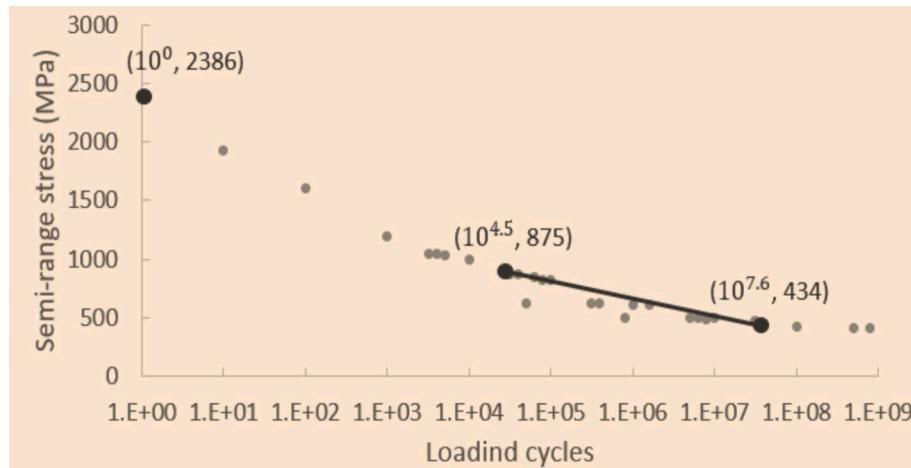
Fig. 5. SN-curve of 100Cr6 steel from torsional fatigue tests (adopted from [29]).

and stress levels at $(10^{4.5}, 875)$ and $(10^{7.6}, 434)$ are selected. This method produces the value of the material constant $m = 10.18$. The stress-axis intercept of the SN-curve, τ_{f1}, can be found to be approximately 2386 MPa. Therefore, the material constant σ_r can be calculated to be approximately 6048 MPa.

To consider the effect of plastic deformation on the damage evolution, the true stress–strain relationship of the 100Cr6 steel after initial yielding is considered in the study, as shown in Fig. 6. It can be determined that the initial yielding stress under compression is approximately 2300 MPa, the Young's Modulus is 220 GPa, and the Poisson's ratio is 0.3.

4.3. Variation of Hertz contact pressure and loading sequences

During the wind turbine operation, the distribution of the Hertz contact pressure applied on the bearing raceway may vary according to the wind speed variation and the overloading conditions such as the shutdown or start-up. To consider the loading magnitude variations, the typical operation condition of a gearbox planetary bearing is divided into 7 loading cases, as shown in Table 1. Case-I to Case-V represent the variation of the maximum Hertz contact pressure when the wind speed changes from 4 m/s to >15 m/s. Case-VI shows the overloading condition during the normal wind turbine start-up and shutdown events. Case-VII presents the overloading condition during some extreme events of the wind turbine operation such as the emergency shutdown or the electrical grid error.
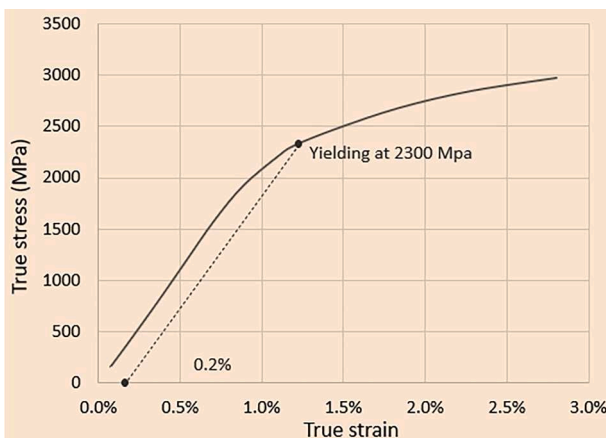

Fig. 6. True stress–strain curve of 100Cr6 steel under compressive loading (data from [38]).

According to the IEC 61400 standards and the published modelling and experimental results in [15,39,40], the values of the maximum Hertz contact pressure acting on the planetary bearing raceway are determined, as shown in Table 1. For the actual operation condition of a wind turbine, the overloading cases may occur at any time throughout the turbine's operation lifetime. Therefore, the overloading conditions may happen at the early or late stages of the bearing operation service. To investigate the effect of loading sequences on the damage initiation and propagation, the term "varying loading group" is proposed. Each loading group has a varied maximum Hertz contact pressure, ranging from 0.92 to 2.84 GPa, as shown in Table 1. The overall loading condition of the bearing raceway may contain more than one loading group. If the multiple loading groups are considered in the overall loading condition, the loading cycles included in each loading group are reduced accordingly.

As discussed in Section 3, the evolution of the damage variable can be evaluated by Eq. (4). If the damage increment is evaluated during every loading cycle by using the developed FE model, it is impossible to simulate the damage accumulation caused by millions of rolling contact loading cycles. As a result, the concept of the "jump-in cycle" introduced by Pandey et al. [41] is applied to calculate the damage accumulation with a large number of rolling contact loading cycles. By employing the jump-in cycle concept, the FE models in this study can calculate the overall damage accumulation during a block of loading cycles instead of a single loading cycle.

According to the experimental results of the twin-discs RCF tests in [11] by Evans et al., when the maximum Hertz contact pressure was approximately 2 GPa and the number of loading cycles is 5.0×10^7, it was found that RCF cracks had already propagated and formed into crack networks in the subsurface area of the 100Cr6 steel. Therefore, the CDM FE models developed in this study are run to simulate the crack initiation and propagation within 2.0×10^7 cycles, at which stage the crack may not propagate into long crack networks. The damage accumulation is computed within every 50,000 cycles ($dN = 5 \times 10^4$, defined as one jump-in cycle), meaning the overall loading cycles of each CDM FE model will have 400 blocks or jump-in cycles to model the overall damage. Additionally, the jump-in cycle concept also assumes that the damage generated during every loading cycle is the same. Thus, the damage accumulation caused by 5×10^4 cycles in one jump-in cycle will be summed up linearly. Considering number of loading groups and jump-in cycles, Fig. 7 shows the jump-in loading cycles in the FE models when one, two and four loading groups, implemented to investigate effects of loading levels and load sequences on the damage evolution.

Table 1
Levels of the maximum contact pressure and loading cycles in each operation loading group.

	Loading case	Maximum contact pressure p_0 (GPa)	Half contact length b (mm)	Contact number percentage
I	4-7 m/s wind speed	0.92	0.236	17.17%
II	7-9 m/s wind speed	1.31	0.335	18.35%
III	9-12 m/s wind speed	1.82	0.392	28.25%
IV	12-15 m/s wind speed	2.06	0.528	11.48%
V	>15 m/s wind speed	2.07	0.531	14.01%
VI	Normal overloading	2.39	0.613	9.60%
VII	Extreme overloading	2.84	0.730	1.15%
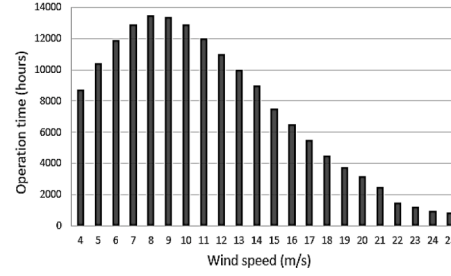
Operation hours of a WT corresponding to the wind speed according to IEC standard 61400-4 (total 161184 hours).
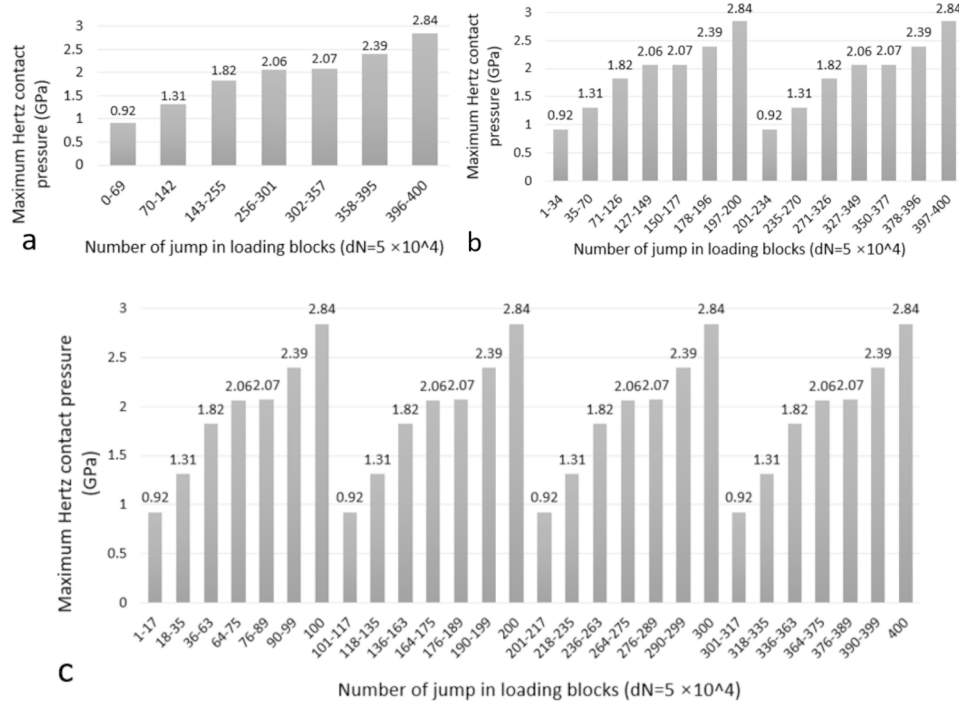
Fig. 7. Definition of jump-in loading blocks considering the loading groups: (a) One loading group. (b) Two loading groups. (c) Four loading groups.

5. Results and discussion

In the following result analysis, the damage parameter, *D*, is shown as the state variable SDV 10. The damage modelling within the inclusion is not considered in this study. Therefore, the crack initiation and propagation from the inclusion only occur within the steel matrix. Due to a number of non-linearity involved in the FE simulation, such as the modelling of the multiple surfaces in contact, microscopic sized inclusions, plastic deformation, and damage accumulation under high RCF loading cycles, the convergence issues frequently occur. In order to achieve a balance between the simulation accuracy and the iterative convergence, the maximum value of the damage parameter D is set to 0.9 in this study. The accumulation of the damage and difference in the crack propagation length are determined by the crack dominating stress ($\tau_{alternating} + |\tau_{mean}|$), defined in Eq. (5), and the crack dominating stress is shown as the state variable SDV 18.

5.1. Evaluation of key factors affecting RCF damage evolution

Fig. 8 shows the equivalent plastic strain results of the steel matrix during the first jump-in cycle, when the maximum Hertz contact pressure is defined as a constant value of 2.069 GPa and the inclusion is perfectly bonded with the steel matrix. The results indicate that the steel matrix is subjected to the plastic deformation during the rolling contact process due to the MnS inclusion, and the equivalent plastic deformation reaches 2.21 %. In this study, the extreme overloading cases, shown in Table 1, can cause the maximum Hertz contact pressure to increase to 2.84 GPa. Under these extreme conditions, the plastic deformation will accumulate and affect the fatigue resistance of the steel matrix. Therefore, it confirms that the consideration of plastic deformation and the back stress of the material in the damage modelling process is necessary to simulate the shakedown and ratchetting processes of the bearing steel under RCF condition.
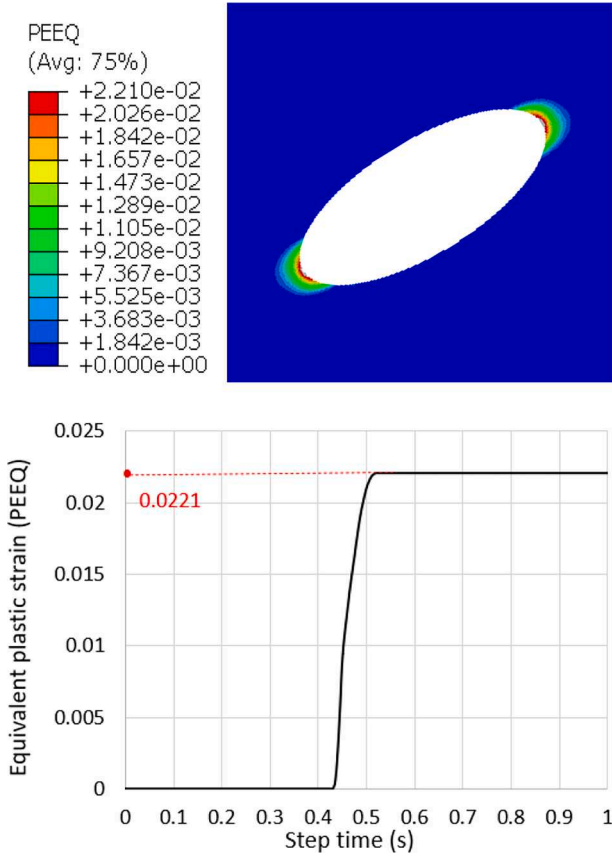
Fig. 8. Equivalent plastic strain of an inclusion perfectly bonded with steel matrix after first jump-in loading cycle.

5.1.1. Effect of inclusion-steel matrix boundary condition

Fig. 9 compares the subsurface RCF damage caused by the MnS inclusion with different boundary conditions. Under the maximum Hertz contact pressure of 2.069 GPa, the maximum traction pressure is 103 MPa when the traction coefficient is 0.05. It can be seen when the inclusion is perfectly bonded with the steel matrix, the accumulated damage D is only 0.235 after 2.0×10^7 loading cycles. This indicates that a perfectly bonded MnS inclusion may not cause great damage to

significantly reduce the bearing fatigue life. However, when the inclusion has a separated boundary or an internal crack, the damaged inclusion has cracks propagated to 3.54 *μm* and 5.67 *μm*, respectively, as shown in Fig. 9(b) and (c). It is clear that the subsurface RCF crack propagation is greatly influenced by the condition of the damaged inclusion when it either has the boundary separation or internal cracking.

As shown in Fig. 10(b), the crack dominating stress at tips of the internally cracked MnS inclusion has reached to 1945 MPa during the first jump-in loading cycle, greater than 1342 MPa when the inclusion is boundary-separated, as shown in Fig. 10(a). Fig. 11 shows the changes in the crack length rate with the increase of jump-in loading cycles for the boundary-separated inclusion and internally cracked inclusion. Because the cracks in the steel matrix are initiated from both tips of the inclusion, only the longer crack is recorded in Fig. 11. The results show that the relationship between the crack length and the loading cycles is not linear. The cracks will propagate more rapidly with the increase of the loading cycles, as shown by the crack propagation rates (da is the slope of the curve sections, averaged over every 100 jump-in cycles). It can be observed that the crack propagation rates for the internally cracked inclusion are greater than the rates for the boundary-separated inclusion. Therefore, the RCF damage accumulation in the steel matrix from an internally cracked inclusion is faster than that from a boundary-separated inclusion, resulting in a greater final crack propagation length. In other words, when compared with the boundary-separated inclusion, the internally cracked inclusion is more harmful to the bearing operating life. Based on the experimental results of a twin-discs test, Bruce et al. [13] reported that the internally cracked inclusions were more likely to occur when the material was subjected to high rolling contact pressures. Therefore, when a butterfly-wing cracking damage is caused by an internally cracked inclusion, it often indicates that the bearing is overloaded during the operation. The increased maximum contact pressure due to the overloading can lead to more severe stress concentration at the subsurface inclusions, which further increases the crack dominating stress leading to a premature failure. Hence, the internally cracked inclusions are very commonly observed in the damaged bearings. The internally cracked inclusions are also important factors resulting in the formation of subsurface crack networks.

5.1.2. Effect of surface traction on damage evolution

It was reported that the surface traction between the bearing rollers and raceways had accelerated the subsurface RCF damage initiation
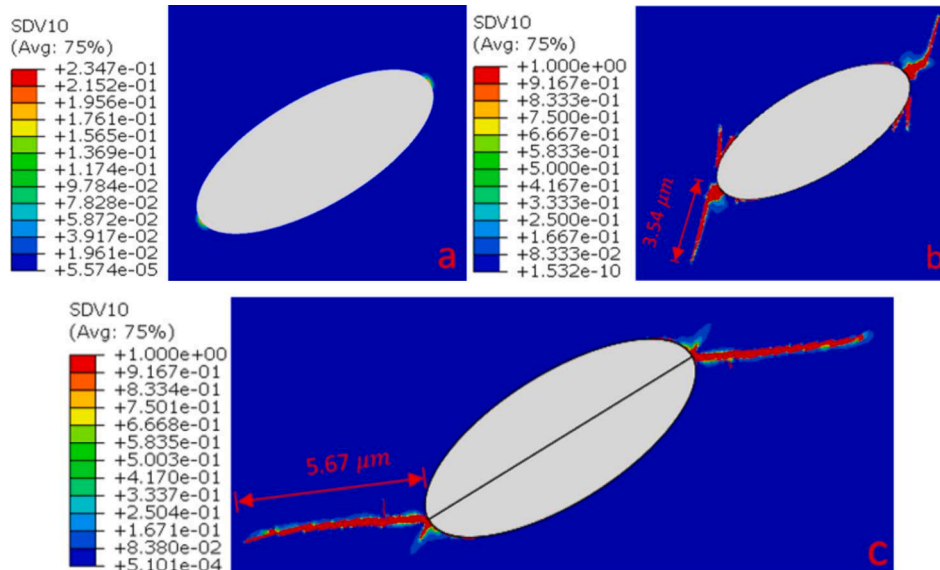

Fig. 9. Conditions of a damaged inclusion on crack propagation: (a) perfectly-bonded inclusion; (b) boundary-separated inclusion; (c) internally-cracked inclusion.
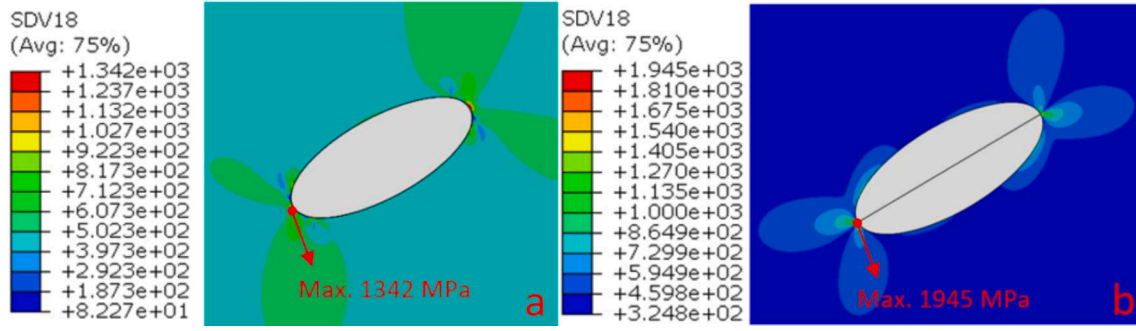
Fig. 10. Comparison of the crack dominating stress (SDV 18) after first jump-in loading cycle when the MnS inclusion has (a) separated boundary (b) internal cracking.
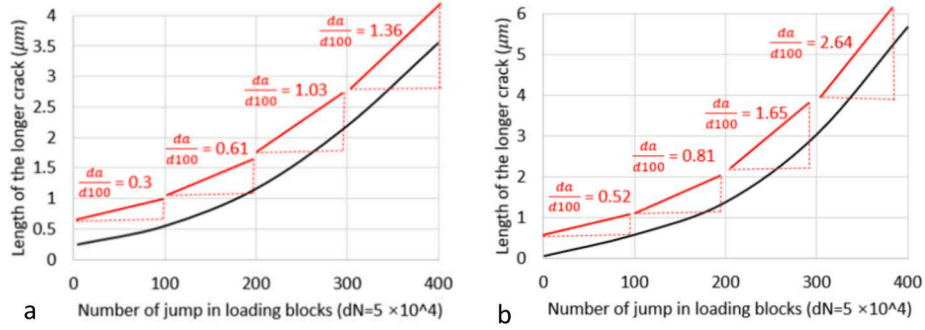

Fig. 11. Crack length vs. jump-in loading cycles: (a) boundary-separated inclusion; (b) internally-cracked inclusion.
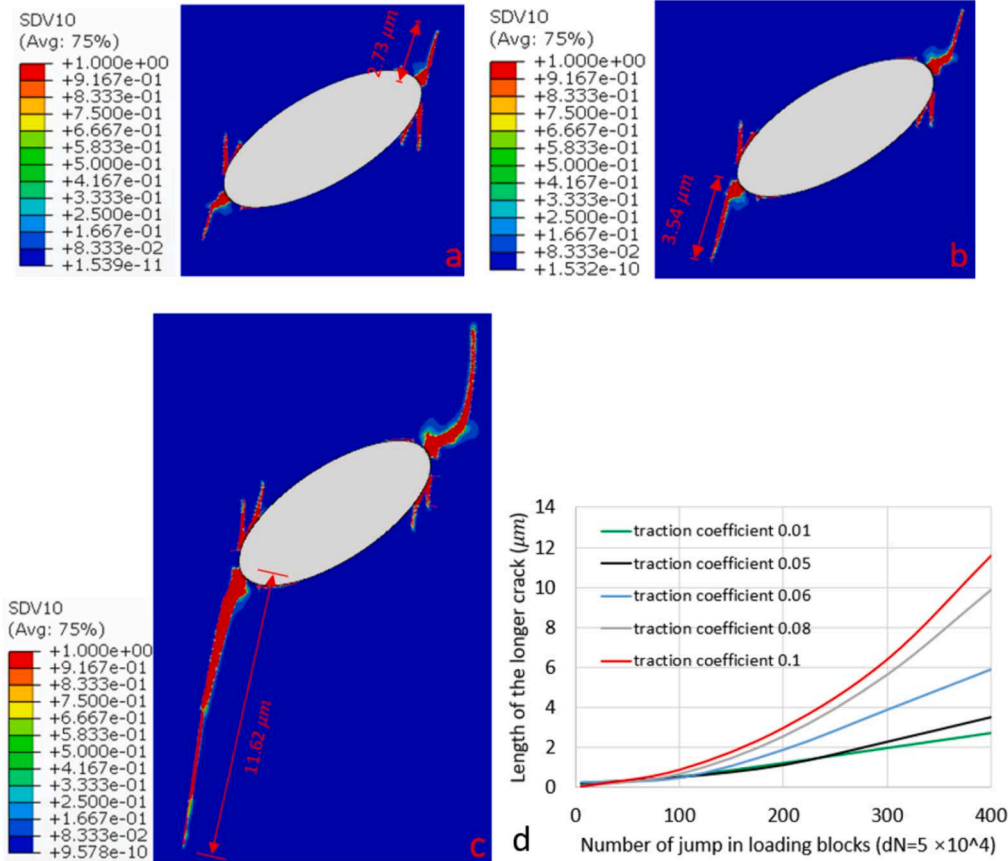

Fig. 12. Evaluation of surface traction on crack propagation when the traction coefficient is varied: (a) 0.01; (b) 0.05; (c) 0.1; and (d) Crack lengths vs. jump-in loading cycles.

[42]. Roller bearings used in the wind turbine gearbox is generally well lubricated thus the traction coefficient between rollers and raceways generally does not exceed 0.1 [13]. Fig. 12 compares the subsurface RCF damage evolution when the traction coefficient is defined as 0.01, 0.05, and 0.1. Because the perfectly bonded inclusions has not led to crack propagation, the inclusion modelled in Fig. 12 is defined as a boundary separated MnS inclusion. With the increase of the traction coefficient, the propagated RCF crack length increases significantly from 2.73 μm to 11.62 μm. Fig. 12(d) shows that the traction coefficient has a significant effect on crack propagation, especially when its value exceeds 0.05.

The FE modelling investigation in [25] and the experimental twin-discs tests in [11] discussed the importance of the traction coefficient on the butterfly-wing crack formation in the wind turbine gearbox bearings. In both studies, it was considered as the factor that made the subsurface maximum shear stress closer to the contact surface. Therefore, some inclusions located very close to the contact surface are more likely to be cracked or boundary separated, leading to the final butterfly-wing crack formation. In addition, due to the positions of these butterfly damage, the cracks have relatively short distances to propagate and to reach the contact surface when compared with other inclusions located deeper in the subsurface of the raceway. The CDM FE modelling results in this study provide supplementary explanations regarding the effect of the traction coefficient on the RCF damage propagation. Inclusions in the relatively deep subsurface area of the raceway may also have high possibilities to initiate the butterfly damage. This is because under an increased orthogonal shear stress, the crack nucleation happens earlier than that under a lower stress condition, which results in a longer propagation period for the crack to reach the contact surface of the raceway. Therefore, it is easier for the crack networks to form from the deep subsurface area and then propagate rapidly to the contact surface under rolling contact loading cycles.

5.1.3. Effect of overloading and loading sequences on damage evolution

Overloading conditions and wind speed variations are very common in the operation of a wind turbine; the fatigue damage initiated from the subsurface area of bearing raceways is likely to occur much earlier than the ultimate failure of bearings. In addition, according to the IEC 61400 standards, a wind turbine can experience thousands of start-up and shutdown events, even in one year's operation. This makes the bearing overloading occur frequently, which further accelerates the propagation of the RCF crack from the subsurface area to the contact surface of the bearing raceway. To evaluate the effect of overloading and extreme loading conditions, Fig. 13 compares the subsurface RCF damage evolution when a varied number of the loading groups is applied to the CDM FE damage model. The model with four loading groups represents that four times more overloading and extreme loading conditions would occur than that in the model with one loading group. As shown in Fig. 13 (a), 13(b) and 13(c), with the increase of the number of loading groups, the propagated RCF crack length increases significantly from 3.36 μm to 11.37 μm. The relationship between the crack length and the jump-in loading cycles is shown in Fig. 13(d). Due to the variation of the maximum Hertz contact pressure from 0.92 GPa to 2.83 GPa in each loading group, cracks in all three CDM FE damage models show the wave-like increasing trends. This is because if the overloading and extreme loading conditions occur earlier in the loading process, cracks initiate earlier from the inclusion and has a longer propagation time to reach the contact surface thus significantly accelerating the damage development.

5.2. Validation of the CDM FE damage model with twin-disc test experiments

To validate the new CDM FE modelling method and the ABAQUS user subroutines developed in this study, additional validation models
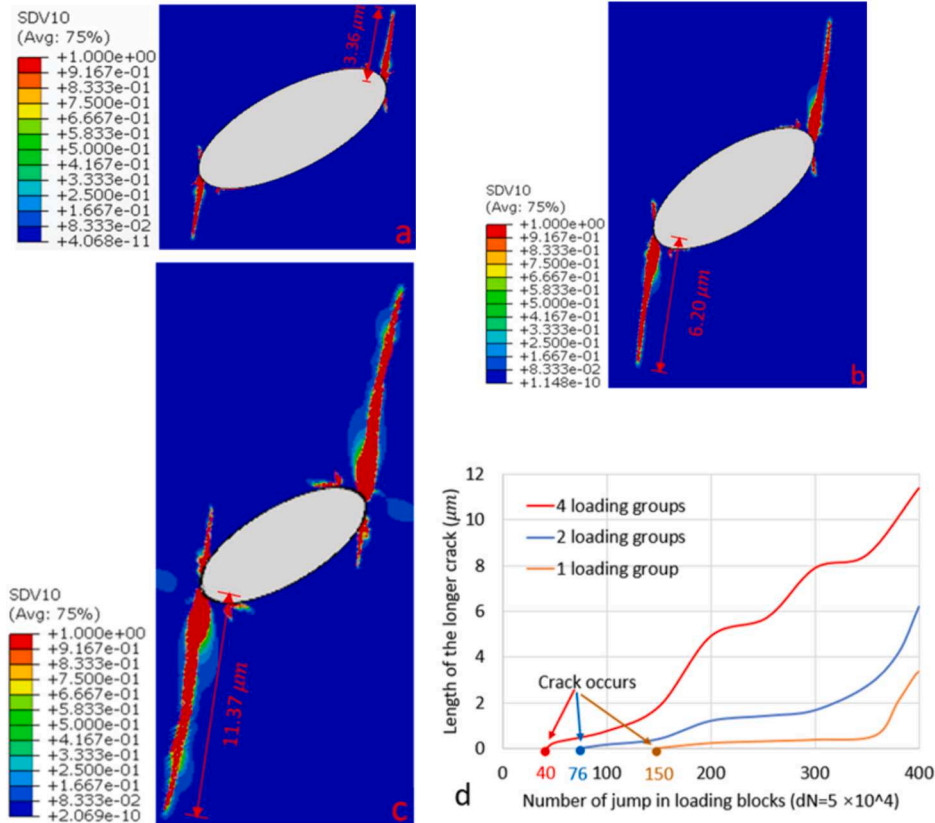

Fig. 13. Evaluation of overloading and extreme loading on crack propagation: (a) 1 loading group; (b) 2 loading groups; (c) 4 loading groups; and (d) comparison of the crack propagation when subjected to 1, 2 and 4 loading groups.

are created for simulating the inclusion-initiated cracks. Fig. 14(a) shows a MnS + Al_2O_3 compound inclusion observed in a damaged 100Cr6 specimen obtained from the twin-disc tests in [11]. Because the inclusion is mostly composed of MnS, for the simplification it is considered as the MnS inclusion in the FE damage modelling. As shown in Fig. 9(a), it has been observed that the perfectly bonded inclusion may not lead to the initiation of cracks in the steel matrix within limited loading cycles. Therefore, although a separated boundary is not visible in Fig. 14(a), it has been assumed that the inclusion and the steel matrix are freely contacted with each other without defining any cohesive behaviour in the FE damage modelling. Using the same testing data in the experiment from [11], the number of overall loading cycles of the CDM FE model is defined as 5×10^7, the maximum contact pressure is 2 GPa, and the traction coefficient is 0.047. Fig. 14(b) shows the simulated crack propagation from the inclusion. The overall length of the butterfly wing cracks modelled is 17.2 μm; while the actual butterfly damage observed from the microscopy is approximately 19 μm. The average angle of two propagated butterfly wing cracks from the FE modelling is 45°, as shown in Fig. 14(b), which is similar to the measured angle of 48° in the microscope image [16]. The modelling results are very close to the actual crack propagation.

Fig. 15(a) shows another MnS + Al_2O_3 compound inclusion observed in the experimental tested specimens in [11]. In the FE damage model, it is also defined as a MnS inclusion with its boundary in free contact with the steel matrix. To facilitate the modelling of the inclusion, the original irregular shape of the inclusion is simplified into an ellipse, as shown in Fig. 15(b). Using the same testing data in the experiment from [11], the overall loading cycles simulated is 2.5×10^7, the maximum contact pressure is 2 GPa, and the traction coefficient is 0.022. As shown in Fig. 15(b), the modelled butterfly damage has a total length of 23.81 μm; while the observed butterfly damage from the experiment is approximated 27 μm. The crack propagation orientation between the experiment and the CDM FE model also has a noticeable difference. As can be observed in Fig. 15(a), the crack has propagated from the inclusion with an average angle of 23° but the FE modelled crack angle is 31°, as shown in Fig. 15(b). These differences may be caused by the simplification of the inclusion geometry in the CDM FE model. Because of this simplification, the crack dominating stress distribution around the inclusion tips may be different from that at the actual inclusion, resulting in the difference of the crack length and the propagation orientation.

As shown in Fig. 16(a), the butterfly-wing cracks, also from the experimental tested specimens in [11], are initiated by a MnS inclusion containing an internal crack. To model an internally cracked inclusion,
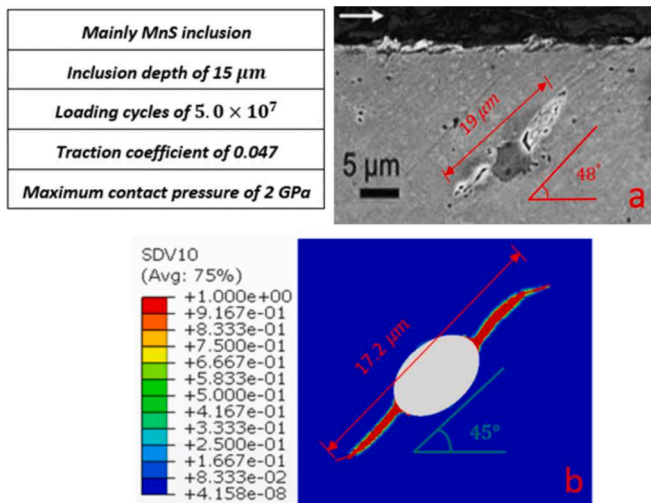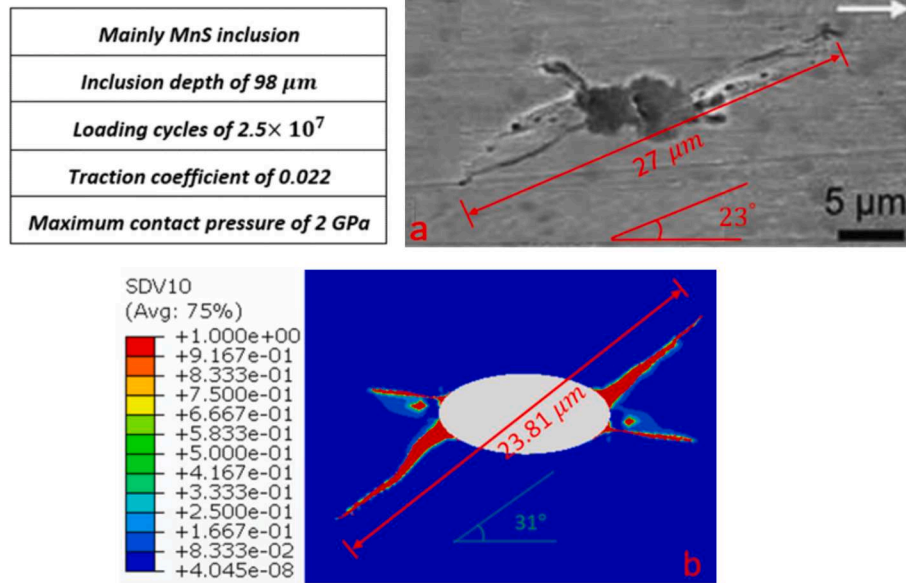
the interface between the inclusion and the steel matrix is defined as perfectly bonded. Using the same testing data in the experiment from [11], the overall loading cycles simulated is 2.5×10^7, the maximum contact pressure is 2 GPa, and the traction coefficient is 0.002. The modelling result of the butterfly-wing cracks is shown in Fig. 16(b). It can be seen that the modelled propagation angle of the cracks is 28° and the measured angle from the experimental tested specimen is 25°. The butterfly-wing cracks propagate exactly by following the direction of the internal crack tips of the inclusion. The modelled overall butterfly crack length is 34.61 μm, which is approximately 4 μm shorter than the butterfly crack length of 39 μm observed in the experimental tested specimen in [11]. This difference may be caused by the definition of the damage parameter D in the CDM FE model. In this study, the maximum value of D is set as 0.9 to avoid the non-convergence problems in the FE simulations. It means that when the accumulated damage parameter exceeds 1.0, ABAQUS software will compulsively change it to 0.9 for the computation of the next jump-in loading cycle. Therefore, in the FE damage modelling, the stress concentration level at the already propagated crack tips should be lower than the actual situation since the FE elements in the cracked area are still withstanding the stress. Consequently, the crack dominating stress in the FE damage modelling is relatively small at the crack tips, leading to the reduction of the propagated crack length. As the difference is small between the modelled and experimentally measured, the effectiveness of the developed CDM FE model is fully demonstrated.

### 5.3. Application of the CDM FE damage model for the failed WT bearing

To further demonstrate the effectiveness of the developed CDM FE method in investigating the accelerated damage development in the WT application, an internally cracked MnS inclusion with butterfly-wing cracks from a failed planetary bearing raceway of a 2 MW WT gearbox in Fig. 1(a), as shown in Fig. 17(a), is used to create the FE damage model. However, the actual loading magnitude and the number of loading cycles experienced by the failed bearing of the WT gearbox in its field operation are not available. Therefore, the overall loading cycle is assumed to be 2×10^7 by employing four varying loading groups assembled from the IEC61400 standards and published studies, as discussed in Section 4.3. The traction coefficient is assumed to be 0.05. As shown in Fig. 17(b), the modelled results of the crack length and propagation angle of the butterfly-wings have some differences with the actual butterfly damage observed from the raceway of the failed bearing. The overall crack length of the butterfly-wings obtained from the CDM FE modelling is 35.9 μm, much shorter than the actual crack length of 54.9 μm. Furthermore, the modelled crack propagation angle 79° is considerably greater than the actual propagation angle of 61°.

Fig. 18(a) shows a butterfly-wing crack network observed in the failed bearing raceway. The damage is caused by two closely located MnS inclusions, which are positioned 817 μm under the contact surface of the bearing raceway. In the definition of the CDM FE model, because the original boundary conditions of the inclusions cannot be identified, the boundaries of both inclusions are defined as free surfaces in contact with the steel matrix. Because the actual loading magnitude and the number of loading cycles experienced by the failed bearing of the WT gearbox in its field operation are not available, in the modelling, the overall loading cycles is assumed to be 2 × 107 by employing four varying loading groups and the traction coefficient is assumed to be 0.05. The modelling results of the butterfly-wing network are shown in Fig. 18(b). It can be seen that the modelled crack propagation angle is 22°, which is close to the actual angle of 24°. However, the actual length of the butterfly is approximately 39 μm, while the butterfly length modelled in the CDM FE is only 10.94 μm.

The differences between the modelling results and the microscopy observations of the crack propagation are most likely resulting from the unknown details of the bearing loading conditions and the sequences of the overloading and extreme loading cases of the operating WT gearbox.

Fig. 14. Comparison of butterfly-wing cracks initiated from MnS inclusion: (a) microscopy image of the inclusion damage from the experiment in [11] (with permission); (b) simulated damage by the developed CDM FE model.

Fig. 15. Comparison of irregular butterfly-wing cracks initiated from MnS inclusion: (a) microscopy image of the inclusion damage from the experiment in [11] (with permission); (b) simulated damage by the CDM FE model.
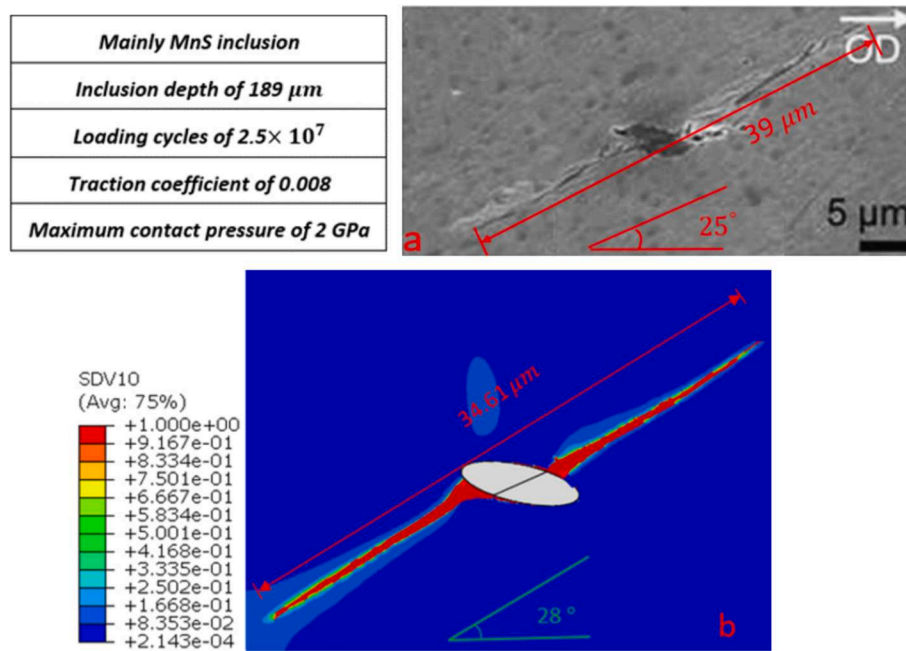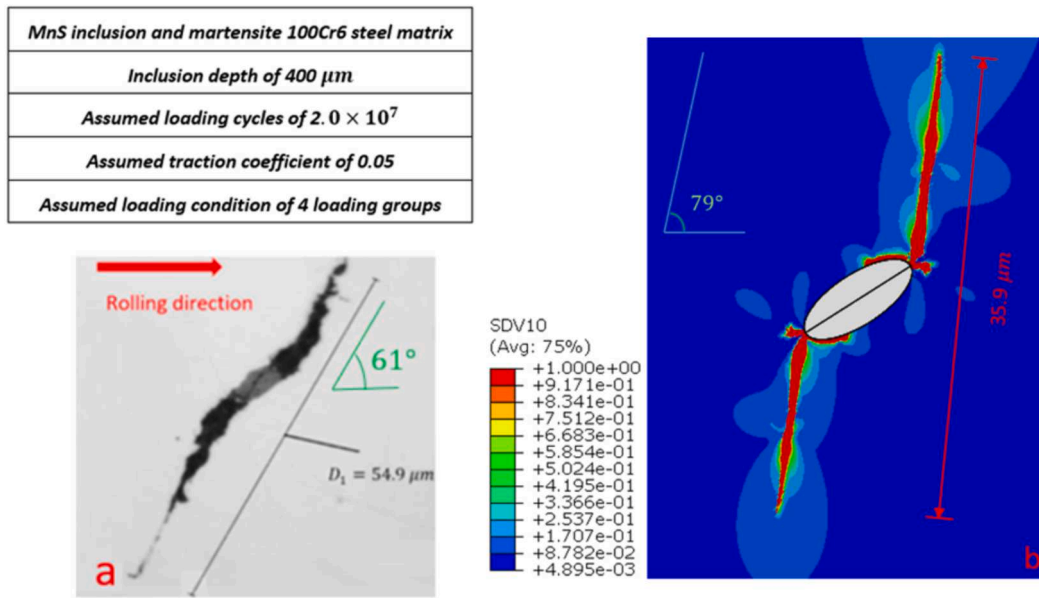

Fig. 16. Comparison of butterfly-wing cracks from an internally cracked MnS inclusion: (a) microscopy image of the inclusion damage from experiment in [11] (with permission); (b) simulated damage by the CDM FE model.

Furthermore, in the FE modelling, the relative position between the inclusion and the applied rolling contact Hertz pressure is assumed to be located in the centre of the FE model which affects the stress concentration around the inclusion and the stress distribution in the subsurface area. Finally, the flaked surface of the raceway, below which the inclusions are modelled in the FE, may affect the contact pressure and the surface traction of the contact zone. Thus the crack dominating stress distribution in the actual subsurface area of the raceway contact zone may be different from that in the FE modelling, contributing to the differences in the crack length and the propagation angle.

The developed CDM FE model demonstrates its effectiveness in predicting both crack initiation and propagation from the damaged inclusions, with boundary separation and internal cracking. This is

evidenced by the validation of the CDM FE model with the results from the twin-disc experimental tests in [11] where the tested loading conditions are available. The application of the developed CDM FE model to the failed WT gearbox bearing shows some differences in length and propagation angle of the butterfly wing cracks, this is mainly caused by the assumed loading conditions in the FE models because the actual loading levels of the 2 MW WT gearbox, including the overloading and extreme loading cases as well as the sequence of these loadings are not available from the WT field operation. As discussed in Section 1 Introduction, it is hypothesised that the accelerated damage evolution and premature failure of the WT gearbox bearings are resulted from the damaged inclusions and complex loading conditions in the WT operation. The results obtained by the CDM FE models have fully

Fig. 17. Comparison of the butterfly-wing cracks from an internally cracked MnS inclusion: (a) damage observed in a failed planetary bearing raceway of the 2 MW WT gearbox; (b) simulated damage by the CDM FE model.
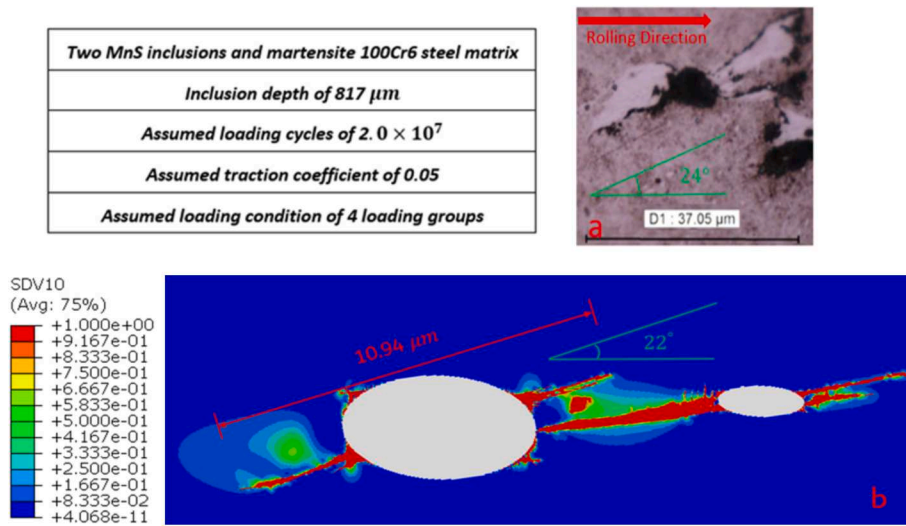
Fig. 18. Comparison of the butterfly-wing crack network from two MnS inclusions: (a) damage observed in a failed planetary bearing raceway of the 2 MW WT gearbox; (b) simulated damage by the CDM FE model.

demonstrated the importance of these critical factors on the accelerated damage evolution, especially the increased frequencies of the over-loading / extreme loading conditions and the early occurrences of these harmful events. In this study, the statistical variations of the wind speed and the occurrence of operational events are determined from the IEC 61400-1:2019 standards and published studies, however, the accurate load data representing the complex operation of WTs is essential to predict the actual damage evolution and premature bearing failure.

6. Conclusions

This study has developed a CDM based FE model to investigate the damage evolution with the accumulation of material plastic deformation and kinematic hardening of the steel matrix around the damaged inclusion due to shakedown and ratchetting processes under rolling contact fatigue. The main conclusions are:

(1) The developed FE model is capable of predicting subsurface inclusion initiated damage and butterfly-wing crack propagation under RCF with varied load levels and loading sequences. The CDM FE model validation of the crack propagations at the damaged inclusions with that obtained in the experiment from [11] has demonstrated the effectiveness and very good accuracy of the developed CDM FE model.

(2) Inclusion damages, including boundary separation and internal cracking, have shown an important effect on the crack initiation and propagation at the inclusion. A perfectly bonded inclusion is less likely to cause the crack initiation within a certain number of loading cycles. However, under the same loading condition, both the internal cracking and boundary separation of an inclusion are found to initiate micro cracks.

(3) It has shown that the traction coefficient only affects the crack propagation length. This effect is not obvious when the traction coefficient is small, varying from 0.01 to 0.05. However, when

the traction coefficient is increased to 0.1, the modelling results indicate that the subsurface cracks caused by the cyclic rolling contact loading have grown rapidly, which may result in the premature failure of the bearing raceways due to the greater growth rate of the cracks.

(4) This study investigates the realistic loading variations caused by the wind speed variation and various operating events. It has been found that the damage of the bearing subsurface has become more severe when the overloading and extreme loading cases occur earlier in the bearing loading process. In other words, the frequent start-ups, shutdowns and emergency stops of the WT operation may result in extremely high stress concentration at damaged inclusions and localised plastic deformation of the steel matrix, leading to the premature failure of the bearing raceways.

(5) The application of the developed FE damage model to predict the butterfly-wing crack propagation at the damaged inclusions of the failed WT gearbox bearing has shown the importance of the critical factors identified in this study. It has confirmed that the complex loading conditions during the WT operation as well as the damaged inclusions have significant effects on the accelerated crack propagation. This study has developed the effective damage modelling method to gain new insights of the complex interactions of these critical factors, which can be utilised to develop new strategies in steel manufacturing and WT operation

to potentially reduce the premature failure and maintenance costs of the WT gearbox bearings.

CRediT authorship contribution statement

R. Dai: Writing – original draft, Visualization, Validation, Methodology, Investigation, Formal analysis, Conceptualization. **H. Long:** Writing – review & editing, Writing – original draft, Supervision, Methodology, Funding acquisition, Conceptualization.

Declaration of competing interest

The authors declare that they have no known competing financial interests or personal relationships that could have appeared to influence the work reported in this paper.

Data availability

Data will be made available on request.

Acknowledgments

Appendix. Calculation of the maximum Hertz contact pressure

Using the parameters of the 2 MW WT gearbox and the upwind planetary bearing shown in Table A1, the maximum Hertz contact pressure between raceway and rolling element of the bearing under the rated WT working condition is determined.

The modelling results obtained from [43] showed that the rotor torque was affected by the wind speed, shown in Fig. A1. The input torque of the rotor under the rated operating conditions can be shown as 1220 *kNm*. With three planetary arms in the gearbox the force acting at the centre of each planet arm can be calculated by

$$F_{pl} = \frac{T_{rotor}}{3 \bullet (D_P + D_S)} \tag{A1}$$

where T_{rotor} is the rotor torque, D_P is the diameter of the planetary gear, and D_S is the diameter of the sun gear, as given in Table A1. The maximum radial load of the upwind bearing can be calculated by

$$Q_{uw} = F_{pl} \bullet L_{\%,uw} \tag{A2}$$

where $L_{\%,uw}$ is the percentage of the loading distributed between the upwind and downwind bearings of the gearbox. LaCava et al. [44,45] found that the upwind bearing normally took 40 %–60 % of the overall radial load. As measured in [45], the load acted on the upwind bearing oscillated from 40 % to 70 % during the operation. In this study, $L_{\%,uw}$ used is 55 %, the mean value obtained in [45]. The maximum radial load acting on rolling elements in the upwind bearing can be calculated by:

$$W_{max} = \frac{5 \bullet Q_{uw}}{i \bullet Z} \tag{A3}$$

where i is the number of sets of rolling elements of the upwind bearing; Z is the number of rolling elements within one set. Given in Table A1, Z is 26, the rollers set of the upwind bearing is 2.

Using Eqs. (A4) and (A5), the maximum Hertz contact pressure and the half contact length under the rated operating condition can be calculated as 2.069 GPa and 0.531 mm, respectively.

$$p_{max} = 0.418\sqrt{W_{max}E/RL} \tag{A4}$$

$$b = \sqrt{4W_{max}R/\pi LE}$$

Table A1

Geometries of the planetary gearbox and upwind planetary bearing.

Planetary gearbox		Upwind planetary bearing	
Number of planetary gears	3	Roller radius R (m)	0.018
Sun gear teeth number N_s	22	Roller length L (m)	0.035
Sun gear pitch diameter (m)	0.25	Inner raceway radius (m)	0.145
Planetary gear teeth number N_P	41	Inner raceway thickness (m)	0.025
Planetary gear pitch diameter (m)	0.465	Number of roller sets	2
Ring gear teeth number N_R	104	Number of rollers within a set	26
Ring gear pitch diameter (m)	1.18	100Cr6: Young's Modulus E	220 GPa
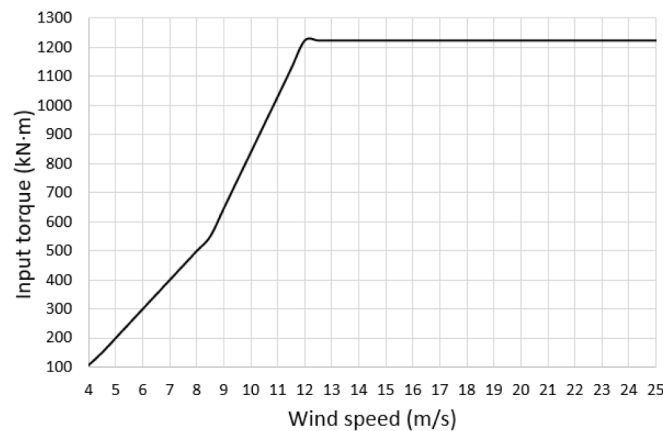
Fig. A1. Input rotor torque vs wind speed [43]

References

[1] Statistics Show Bearing Problems Cause the Majority of Wind Turbine Gearbox Failures. Department of Energy; 2015. <https://www.energy.gov/eere/wind/articles/statistics-show-bearing-problems-cause-majority-wind-turbine-gearbox-failures> [accessed February 2024].
[2] Evans M-H. An updated review: white etching cracks (WECs) and axial cracks in wind turbine gearbox bearings. Mater Sci Technol 2016;32(11):1133–69. https://doi.org/10.1080/02670836.2015.1133022.
[3] Garabedian NT, Gould BJ, Doll GL, Burris DL. The cause of premature wind turbine bearing failures: overloading or under loading? Tribol Trans 2018;61(5):850–60. https://doi.org/10.1080/10402004.2018.1433345.
[4] Sheng S, Keller J, Greco NA, Cotrell J, Greco A. Wind turbine drivetrain reliability collaborative workshop a recap; 2016. <https://doi.org/10.2172/1314863>.
[5] International Organisation for Standardisation. BS ISO 15243 : 2017 BSI standards publication rolling bearings - damage and failures - terms, characteristics and causes. vol. ISO 15243; 2017.
[6] Errichello RL. Morphology of Micropitting. AGMA Tech Paper, Gear Technol 2011; 4:74–81.
[7] Evans M-H, Richardson AD, Wang L, Wood RJK. Serial sectioning investigation of butterfly and white etching crack (WEC) formation in wind turbine gearbox bearings. Wear 2013;302(1–2):1573–82. https://doi.org/10.1016/j.wear.2012.12.031.
[8] Bruce T, Rounding E, Long H, Dwyer-Joyce RS. Characterisation of white etching crack damage in wind turbine gearbox bearings. Wear 2015;338–339:164–77. https://doi.org/10.1016/j.wear.2015.06.008.
[9] Gould B, Greco A. Investigating the process of white etching crack initiation in bearing steel. Tribol Lett 2016;62(2):1–14. https://doi.org/10.1007/s11249-016-0673-z.
[10] Šmeļova V, Schwedt A, Wang L, Holweger W, Mayer J. Microstructural changes in White Etching Cracks (WECs) and their relationship with those in Dark248 Etching Region (DER) and White Etching Bands (WEBs) due to Rolling Contact Fatigue (RCF). Int J Fatigue 2017;100:148–58. https://doi.org/10.1016/j.ijfatigue.2017.03.027.
[11] Evans MH, Richardson AD, Wang L, Wood RJK. Effect of hydrogen on butterfly and white etching crack (WEC) formation under rolling contact fatigue (RCF). Wear 2013;306(1–2):226–41. https://doi.org/10.1016/J.WEAR.2013.03.008.
[12] Ruellan A, Cavoret J, Ville F, Kleber X, Liatard B. Understanding white etching cracks in rolling element bearings: State of art and multiple driver transposition on a twin-disc machine. Proc Inst Mech Eng Part J J Eng Tribol 2017;231(2):203–20. https://doi.org/10.1177/1350650116648058.
[13] Bruce T, Long H, Dwyer-Joyce RS. Threshold maps for inclusion-initiated micro-cracks and white etching areas in bearing steel: the role of impact loading and surface sliding. Tribol Lett 2018;66(3):pp. https://doi.org/10.1007/s11249-018-1068-0.
[14] Manieri F, Stadler K, Morales-Espejel GE, Kadiric A. The origins of white etching cracks and their significance to rolling bearing failures. Int J Fatigue 2019;120:107–33. https://doi.org/10.1016/j.ijfatigue.2018.10.023.
[15] Bruce T, Long H, Dwyer-Joyce RS. Dynamic modelling of wind turbine gearbox bearing loading during transient events. IET Renew Power Gener 2015;9(7):821–30. https://doi.org/10.1049/iet-rpg.2014.0194.
[16] Al-Tameemi HA, Long H, Dwyer-Joyce RS. Damage characterisation of white etching cracks in a black oxide coated wind turbine gearbox bearing. Wear 2019; 432–433:102923. https://doi.org/10.1016/j.wear.2019.05.038.
[17] Lund TB. Sub-surface initiated rolling contact fatigue-influence of non-metallic inclusions, processing history, and operating conditions. J ASTM Int 2010;7(5). https://doi.org/10.1520/JAI102559.
[18] Richardson AD, Evans MH, Wang L, Wood RJK, Ingram M, Meuth B. The Evolution of White Etching Cracks (WECs) in rolling contact fatigue-tested 100Cr6 steel. Tribol Lett 2018;66(1):6. https://doi.org/10.1007/S11249-017-0946-1.
[19] Vincent A, Lormand G, Lamagnère P, Gosset L, Girodin D, Dudragne G, et al. From white etching areas formed around inclusions to crack nucleation in bearing steels under rolling contact fatigue. ASTM Spec Tech Publ 1998;1327:109–23. https://doi.org/10.1520/STP12123S.
[20] Alley ES, Neu RW. Microstructure-sensitive modelling of rolling contact fatigue. Int J Fatigue 2010;32(5):841–50. https://doi.org/10.1016/J.IJFATIGUE.2009.07.012.
[21] Ravi G, De Waele W, Hertelé S. Numerical methodology to predict subsurface crack initiation from non-metallic inclusions due to rolling contact fatigue. Springer Singapore 2021. https://doi.org/10.1007/978-981-15-9893-7_33.
[22] Mahdavi H, Poulios K, Kadin Y, Niordson CF. Finite element study of cyclic plasticity near a subsurface inclusion under rolling contact and macro-residual stresses. Int J Fatigue 2021;143:105981. https://doi.org/10.1016/J.IJFATIGUE.2020.105981.
[23] Mahdavi H, Poulios K, Kadin Y, Niordson CF. On the effect of microplasticity on crack initiation from subsurface defects in rolling contact fatigue. Int J Fatigue 2022;161:106870. https://doi.org/10.1016/j.ijfatigue.2022.106870.
[24] Mobasher Moghaddam S, Sadeghi F, Weinzapfel N, Liebel A. A damage mechanics approach to simulate butterfly wing formation around nonmetallic inclusions. J Tribol 2014;137(1):011404. https://doi.org/10.1115/1.4028628.
[25] Al-Tameemi HA, Long H. Finite element simulation of subsurface initiated damage from non-metallic inclusions in wind turbine gearbox bearings. Int J Fatigue 2020; 131:105347. https://doi.org/10.1016/J.IJFATIGUE.2019.105347.
[26] Kachanov LM. Rupture time under creep conditions. Int J Fract 1999;97(1–4):pp. https://doi.org/10.1023/A:1018671022008.
[27] Xiao YC, Li S, Gao Z. A continuum damage mechanics model for high cycle fatigue. Int J Fatigue 1998;20(7):503–8. https://doi.org/10.1016/S0142-1123(98)00005-X.

[28] Wang M, Fei Q, Zhang P. A modified fatigue damage model for high-cycle fatigue life prediction. Adv Mater Sci Eng 2016;2016. https://doi.org/10.1155/2016/2193684.

[29] Raje N, Sadeghi F, Rateick RG, Engines JP. A statistical damage mechanics model for subsurface initiated spalling in rolling contacts; 2008. doi: 10.1115/1.2959109.

[30] Li F, Hu W, Meng Q, Zhan Z, Shen F. A new damage-mechanics-based model for rolling contact fatigue analysis of cylindrical roller bearing. Tribol Int 2018;120:105–14. https://doi.org/10.1016/j.triboint.2017.12.001.

[31] Marghitu DB, Diaconescu CI, Ciocirlan BO. Mechanics of Materials. Mechanical Engineer's Handbook 2001:119–88. https://doi.org/10.1016/B978-012471370-3/50004-8.

[32] Biot MA. Mechanics of incremental deformations; 1965.

[33] Sadeghi F, Jalalahmadi B, Slack TS, Raje N, Arakere NK. A review of rolling contact fatigue. J Tribol 2009;131(4):041403. https://doi.org/10.1115/1.3209132.

[34] Chaboche JL. On some modifications of kinematic hardening to improve the description of ratchetting effects. Int J Plast 1991;7(7):661–78. https://doi.org/10.1016/0749- 6419(91)90050-9.

[35] Al-Tameemi HA, Long H, Dwyer-Joyce RS. Initiation of sub-surface micro-cracks and white etching areas from debonding at non-metallic inclusions in wind turbine gearbox bearing. Wear 2018;406–407:22–32. https://doi.org/10.1016/j.wear.2018.03.008.

[36] Kusche CF, Gibson JSKL, Wollenweber MA, Korte-Kerzel S. On the mechanical properties and deformation mechanisms of manganese sulphide inclusions. Mater Des 2020;193:108801. https://doi.org/10.1016/J.MATDES.2020.108801.

[37] Helou T, Wessel U, Vaschetti LL. Tribological behaviour of MnS and MnS compounds in friction material for passenger cars. SAE Techn Pap 2003. https://doi.org/10.4271/2003-01-3315.

[38] Ellermann A, Scholtes B. The strength differential effect in different heat treatment conditions of the steels 42CrMoS4 and 100Cr6. Mater Sci Eng A 2015;620:262–72. https://doi.org/10.1016/j.msea.2014.10.027.

[39] Greaves PR, Dominy RG, Ingram GL, Long H, Court R. Evaluation of dual-axis fatigue testing of large wind turbine blades. Proc Inst Mech Eng C J Mech Eng Sci 2012;226(7):1693–704. https://doi.org/10.1177/0954406211428013.

[40] Guo Y, Keller J, Lacava W. Planetary gear load sharing of wind turbine drivetrains subjected to non-torque loads. Wind Energy 2015;18(4):757–68. https://doi.org/10.1002/WE.1731.

[41] Pandey VB, Singh IV, Mishra BK, Ahmad S, Venugopal Rao A, Kumar V. A new framework based on continuum damage mechanics and XFEM for high cycle fatigue crack growth simulations. Eng Fract Mech 2019;206:172–200. https://doi.org/10.1016/J.ENGFRACMECH.2018.11.021.

[42] Olver AV. The mechanism of rolling contact fatigue: an update. 2006; 219(5):313–330. doi: 10.1243/135065005X9808.

[43] Berthelsen TL, Cordero A, Døhlie JK, Pedersen KU. Intelligent start-up of wind turbines; 2011. p. 105.

[44] Lacava W, Keller J, McNiff B. Gearbox reliability collaborative: test and model investigation of sun orbit and planet load share in a wind turbine gearbox. In: Collection of technical papers - AIAA/ASME/ASCE/AHS/ASC structures structural dynamics and materials conference; 2012. https://doi.org/10.2514/6.2012-1418.

[45] LaCava W, Xing Y, Marks C, Guo Y, Moan T. Three-dimensional bearing load share behaviour in the planetary stage of a wind turbine gearbox. IET Renew Power Gener 2013;7(4):359–69. https://doi.org/10.1049/IET-RPG.2012.0274.